



Predictive modelling of seismic properties in single-foliated slates

Marco A. Lopez-Sánchez^{a,*¹}, Víctor Cárdenes^a, Fabrice Barou^b, Sergio Llana-Fúnez^a

^a Departamento de Geología, Universidad de Oviedo, 33005 Oviedo, Spain

^b Géosciences Montpellier – CNRS & Université de Montpellier, Montpellier, France

ARTICLE INFO

Keywords:

Slate
Crystallographic Preferred Orientation
Seismic properties
Seismic anisotropy

ABSTRACT

Slates play a key role in understanding the seismic anisotropy of the continental crust, a crucial aspect of geophysical interpretation. Using a comprehensive set of high-quality single-foliated chlorite-bearing roofing slates, we determined their typical seismic properties via mineral fractions and orientation distribution functions using the geometric mean averaging method. Our study focused on identifying an optimal transverse isotropy (polar) model, assess correlations between elastic constants, and explore the feasibility of predicting intrinsic maximum anisotropy from a single proxy. We demonstrate that maximum axial and polarization anisotropy in single-foliated slates can be accurately estimated with ~10 % error using a single proxy, termed the S-norm, which integrates the ODF strength and volumetric fraction of phyllosilicates. Additionally, we found that a polar parameterization combining elastic tensor decomposition and the Anderson equations yields seismic anisotropy predictions similar to the Christoffel equation, with errors below 2.8 % (better than 0.2 % for Vp anisotropy). Lastly, our findings suggest that it is feasible to estimate the seismic properties of transversely isotropic slates from only two elastic measurements: a diagonal component and the non-diagonal C13 component. These models are applicable for investigating slate belts at various depths, enabling the calculation of the minimum expected seismic anisotropy from intrinsic properties.

1. Introduction

Slates, a major component of continental crust and sedimentary basins, play a key role in seismic wave propagation and fluid flow due to their pronounced seismic anisotropy and low permeability. Alongside serpentinites (e.g. Ji et al., 2013; Jung, 2011; Katayama et al., 2009; Kern et al., 2015; Wenk et al., 2025), mica-rich schists, mylonites and gneisses (e.g. Godfrey et al., 2000; Ivankina et al., 2017; Ji et al., 2015; Mainprice and Casey, 1990; Meltzer and Christensen, 2001; Ward et al., 2012), slates are among the few crustal rocks capable of developing strong intrinsic seismic anisotropy (exceeding 10 %) (Wenk et al., 2020). This makes them a plausible source for the seismic anisotropy and shear wave splitting observed in the continental crust (Acevedo et al., 2022; Barruol et al., 1998; Barruol and Mainprice, 1993; Cholach et al., 2005; Christensen and Mooney, 1995; Díaz et al., 2006; Lloyd et al., 2009).

Despite their volumetric significance and unique seismic fingerprint, most seismic property studies on phyllosilicate-rich rocks have primarily focused on shales due to their economic importance in the petroleum industry (e.g., Asaka et al., 2021; Hornby, 1998; Johnston and

Christensen, 1995; Lonardelli et al., 2007; Sayers, 2005; Yurikov et al., 2021). This has led to a notable imbalance in the research conducted on the seismic properties between shales and slates. Although shales are the precursors of slates, it remains unclear whether the seismic properties of shales can be directly extrapolated to slates, given that metamorphic processes can enhance or diminish their anisotropic properties. This research paper aims to fill this gap by determining the typical seismic properties of chlorite-bearing single-foliated slates and to test which models are best suited to predict their seismic properties.

The general microstructure and the typical crystallographic preferred orientation (CPO) of the primary mineral phases in slates are well documented (e.g., Wenk et al., 2020 and references therein). Phyllosilicates in slates can develop exceptionally strong CPOs, with c-axis orientation peaks in pole figure two orders of magnitude higher than a uniform crystallographic orientation. Specifically, in single-foliated slates, phyllosilicate c-axis (i.e., the slow direction) arranges normal to the slaty cleavage and the a- and b-axes (fast directions) arrange randomly within the cleavage plane. In contrast, quartz and feldspars tend to show either a random or a weak preferred orientation

* Corresponding author.

E-mail address: marco.lopez@csic.es (M.A. Lopez-Sánchez).

¹ Now at: Instituto Andaluz de Ciencias de la Tierra (IACT-CSIC), Consejo Superior de Investigaciones Científicas, 18100, Armilla, Granada, Spain.

of crystallographic axes despite the development of flattened shapes, i.e. there is a complete decoupling between shape and crystallographic orientation.

The unique arrangement of major minerals in slates, coupled with their high phyllosilicate content and the strongly anisotropic seismic properties of phyllosilicates, provides these rocks their distinct transversely isotropic seismic fingerprint and the ability to reach exceptionally high axial anisotropy values. Reported maximum seismic anisotropy values vary widely between 5 and 66 % for Vp, 5 to 47 % for Vs1, and 5 to 30 % for shear wave splitting (Cárdenes et al., 2021; Guo et al., 2014; Naus-Thijssen et al., 2011b; Wenk et al., 2022). These exceptionally wide ranges of anisotropy reflect the combined effects of intrinsic factors (mineral content and crystallographic orientation) and extrinsic factors, such as the effect of porosity, oriented cracks, shape fabric, or the elastic properties of the interplatelet medium. For single-foliated slates, it is well established that extrinsic factors tend to increase axial anisotropy values by further reducing wave propagation velocity in directions normal to the foliation (Cárdenes et al., 2021, see also fig. S4 in Supplementary material). Conversely, the impact of extrinsic microscale factors (e.g., porosity, oriented cracks) in slates and serpentinites tends to be negligible at pressures above 150 MPa (approximately 6 km burial depth) (Cholach et al., 2005; Guo et al., 2014; Ji et al., 2013). Thus, the anisotropy of slate can be primarily controlled by intrinsic factors, distinguishing them from shales.

Using a diverse set of high-quality (i.e. suitable for roofing) chlorite-bearing single-foliated slates with varying arrangements (grains sizes, shape fabrics, etc.) and mineral fractions, and large area EBSD mapping (including thousands of grains), our aim is to explore the limits imposed by the intrinsic factors on the seismic properties of slates, and to establish a robust model for calculating slate anisotropy based on simple proxies.

2. Materials and methods

2.1. Samples

Our analysis included 14 single-foliated Chl-bearing slates, which belong to different varieties of “roofing slates” (i.e. used as tiles for roofs and covers) with varying metamorphic degrees collected in operative quarries around the world (Table 1). In addition, we included a micaeous quartzite (ALT) for comparison. The slate samples PBT, WA, RIM, RVS, and BRA had not been previously analysed, while the ANL, BEI, CA, EUP GXE, IRO, and OSO samples were previously modelled in Cárdenes

Table 1
Location, lithology and metamorphic degree (Kübler index) of the sample set.

Sample	Location	Type	Kübler Index/Met. Zone
BRA	Pompeu, Minas Gerais, Brasil	metallutite	0.37 (Anchizone)
CA	O Courel, Lugo, Spain	slate	0.37 (Anchizone)
WA	Neufchâteau, Luxembourg, Belgium	slate	0.31 (Anchizone)
IRO	Valdeorras, Ourense, Spain	slate	0.28 (Anchizone)
RIM	Rimogne, Ardennes, France	slate	*Anchizone
PBT	Peach Bottom, Pennsylvania, USA	slate (phyllonite)	*Epizone
BEI	Beira do Rio, Lugo, Spain	phyllite	*Epizone
GXE	Bretaña, Lugo, Spain	phyllite	0.22 (Anchizone)
EUP	Vilarello, Lugo, Spain	slate	0.18 (Anchizone)
OSO	Bretaña, Lugo, Spain	phyllite	0.15 (Anchizone)
ANL-II	Anllares, León, Spain	slate	0.09 (Anchizone)
RVS	La Florida, San Luis, Argentina	phyllite	0.05 (Anchizone)
ALT	Alta, Finnmark, Norway	mica-bearing quartzite	*Epizone

* Kübler index (illite crystallinity) not measured, metamorphism based on mineral association.

et al. (2021). We reanalysed these samples because the mineral content in Cárdenes et al. (2021) was based on EBSD data, which resulted in lower than actual phyllosilicate fractions due to uneven EBSD indexing between phases. In this study, we re-estimated the phyllosilicate/silt fractions based on chemical maps (see section 2.2). Additionally, for quartz and chlorite we used more recent elastic constants in the modelling (Table 2). The difference is particularly noticeable in the case of chlorite, which exhibits less elastic anisotropy and more pronounced axial symmetry than the one used in Cárdenes et al. (2021). The Vp and Vs1 wave speeds of these samples were measured experimentally at room pressure conditions in Cárdenes et al. (2021) and are thus useful for validating the modelling procedure developed here. Lastly, larger EBSD maps have been measured for the IRO and OSO samples.

2.2. Methods

2.2.1. Petrological characterization and metamorphic degree

Petrological characterization was carried out on a single thin section of each sample using optical and electron microscopy. To quantify the metamorphic grade of the slates, the Kübler index, which measures metamorphic grade based on illite crystallinity, was determined (Table 1, Fig. 1c) by X-ray diffraction at the Analytical Services facilities of the University of Extremadura, Spain, following the protocol established by the IGPC Working Group 294 IC (Fettes and Desmons, 2011).

2.2.2. Mineral fraction estimation

Mineral content was quantified using large-area multi-elemental Energy Dispersive X-ray Spectroscopy (EDS) chemical maps acquired from a single section, either XZ or XY sections (Table 3), which may result in minor biases in the calculation of the mineral modal content. Details of the procedure and the custom Python codes used are available in the Supplementary Material.

2.2.3. Electron backscatter diffraction (EBSD) acquisition and data processing

For EBSD analysis, we extracted a 2 × 2 cm slab from each sample and embedded in epoxy resin at room pressure with the XZ or XY plane facing upwards. Polishing was achieved with diamond paste down to 0.25 µm, followed by a final polish using colloidal silica in a VibroMet polisher. EBSD and EDS maps were acquired simultaneously using a CamScan X500-FE CrystalProbe SEM at Géosciences Montpellier (France) to determine both the crystallographic preferred orientation of minerals and their phase composition. We analysed the samples with no carbon coating under low vacuum conditions (~5 Pa). The operating conditions for EBSD acquisition included an accelerating voltage of 20 kV and a working distance of 24–25 mm. EBSD patterns were indexed using HKL Technology’s AZtec v3.2 software at a rate of about 40 Hz. Angular resolution is better than 0.5 degrees.

Table 2

Summary of single-crystal elastic properties, densities and references used for the modelling.

Mineral	Density (g/cm ³)	Elastic constants source	Method
α-Quartz	2.648	Wang et al. (2015)	Brillouin scattering
Low albite	2.623	Brown et al. (2006)	Brillouin scattering
Muscovite	2.830	Militzer et al. (2011)	Atomic first-principles (DFT-LDA)
Chlorite	2.71*	Mookherjee and Mainprice (2014)	Atomic first-principles (DFT-GGA)
Chloritoid	3.100	Lee et al. (2021)	Atomic first-principles (DFT-GGA)
K-feldspar	2.555	Waesimalmann et al. (2016)	Impuls stimulated scattering
Epidote	3.440	Bass (2013)	Ultrasonic pulse transmission

* Averaged from several clinochlores in Katahara (1996).

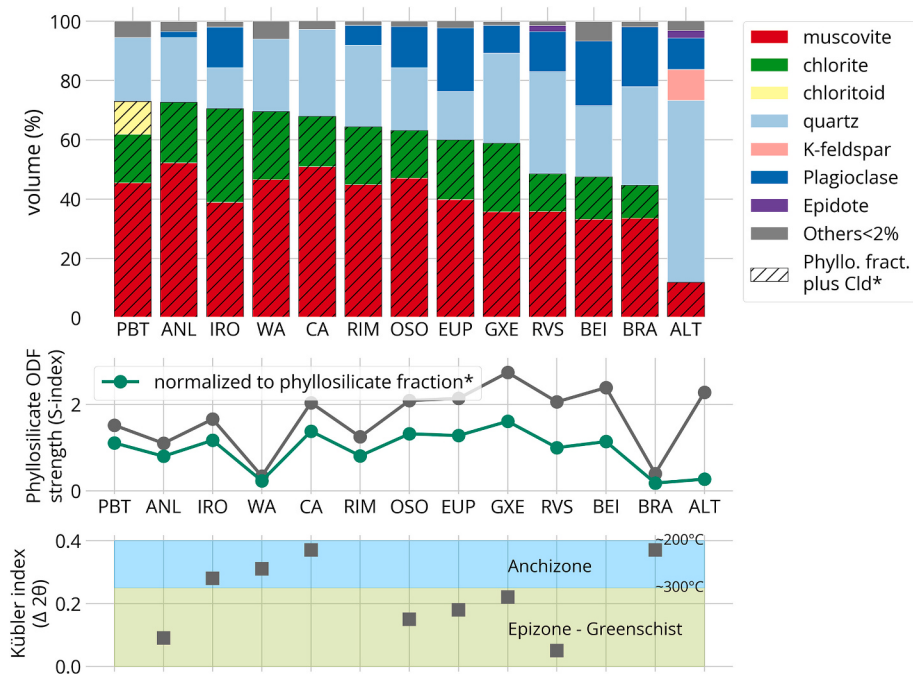


Fig. 1. Mineral composition, phyllosilicate preferred orientation, and degree of metamorphism. (a) Volumetric contribution of the major mineral phases estimated using large-coverage EDS chemical maps. The hatched area represents the volumetric contribution of the phyllosilicates excepting in sample PBT where chloritoid (11.1 %) is also included (see section 3.2 for details). Sample ALT is a micaceous quartzite with 11.9 % of micas. The remaining samples are single-foliated slates with phyllosilicate content varying between 72.6 and 44.6 %. Only mineral phases above 2 % are considered for computing seismic properties. A table with volume fraction values is provided in the Supplementary Material as Table S4. (b) Phyllosilicate CPO intensity, measured by the S-index (orientation entropy in Euler space), both raw and normalised to the total phyllosilicate fraction (Table S5). (c) The degree of metamorphism for most of the slates using the Kübler index (illite crystallinity) (Table 1).

Table 3
EBSD map properties.

Sample	area (mm ²)	step size (μm)	total indexing rate (%)	Section	Chl indexing rate (%) [*]	Ms indexing rate (%) [*]	num. Phases	Ms grains	Chl grains	Qtz grains	Pl grains
ALT	6.4993	3.00	95.5	XZ	–	71	10	3392	–	5411	2231
ANL-II	1.2009	0.70	73.8	XZ	78	35	7	16,126	15,780	27,475	1047
BEI	0.5336	0.80	86.8	XZ	98	72	8	6435	5072	1774	2244
BRA	0.4526	1.00	47.3	XY	7	5	10	392	204	9072	2624
CA	1.2009	0.70	79.2	XZ	99	39	7	16,703	21,371	28,548	–
EUP	0.8337	0.80	79.4	XZ	70	53	9	13,227	8906	6349	8687
GXE	0.5336	0.80	73.0	XZ	39	34	6	4842	2730	9327	2071
IRO-2021	2.1000	0.80	75.2	XY	54	64	12	26,333	28,838	11,602	4325
OSO-2021	0.2962	0.80	72.0	XY	69	81	8	2497	1402	805	759
PBT	0.5279	0.75	54.3	XZ	21	10	12	1512	1180	6155	–
RIM*	0.8802	0.80	45.4	XZ	3	4	12	10,702	4867	7446	1631
RVS	1.1874	0.65	56.3	XZ	16	8	10	2748	2256	6410	6491
WA	1.1512	0.64	60.8	XZ	11	28	12	10,653	2943	31,182	–

* Estimated by comparing the surface area occupied by chlorite and muscovite in the EDS maps and their surface area indexed in EBSD.

EBSD map step sizes (spatial resolution) ranged from 0.64 to 3 μm, covering areas between 0.6 × 0.5 and 2.5 × 2.6 mm² depending on grain size, and included thousands of grains per major mineral to ensure representative sampling (Table 3; see EBSD maps in Supplementary material). We used small step sizes to reconstruct grain boundaries reliably, even when indexing was suboptimal, especially for phyllosilicates. Indexing success ranged from 45.4 % to 95.5 %, with 60 % of maps exceeding 70 % (Table 3). Phyllosilicate indexing varied widely, from >99 % for chlorite in the CA sample to 3–4 % for muscovite and chlorite in the RIM sample (Table 3).

To process the EBSD data after acquisition, we used the MTEX toolbox v5.10.2 (Mainprice et al., 2015) with examples provided in the Supplementary Material. Briefly, we excluded orientation data with a

Mean Angular Deviation (MAD) exceeding 1.3 and removed any wild spikes. We then segmented grains using a Voronoi decomposition algorithm with a misorientation threshold set at 10° and remove all grains with less than four pixels. The Crystallographic Preferred Orientations (CPO) are depicted in upper-hemisphere contour pole figures, illustrating volume/area-weighted orientations. CPOs in pole figures are expressed in multiples of a uniform distribution (m.u.d.), where 1 m.u.d. corresponds to a uniform distribution (lack of preferred orientation). The m.u.d. value depends on the kernel size chosen for its calculation and values obtained by different authors may not be comparable. Thus, m.u.d. values are only here for qualitative comparison between samples.

We quantified the CPO strength for each mineral phase using the Orientation Distribution Function (ODF) and two proxies that measure

the deviation of the ODF from a uniform distribution. The first proxy is the J-index, the L2 norm (i.e. square root of the sum of squared values) of the ODF, which reflects the concentration of orientations in 3D Euler space. This metric ranges from one (uniform distribution) to infinity (single orientation) (Bunge, 1982; Mainprice et al., 2015). The second is the S-index, based on the entropy of the ODF, introduced by Schaeben (1988). It quantifies the degree of organization in orientation (3D Euler) space, ranging from 0 (uniform) to negative infinity (single orientation). Here, we used the absolute value of the entropy so that higher values indicate stronger CPO. The relationship between J and S is complex, S is more sensitive to small intensity ODF values (Hielscher et al., 2007). For further details on their calculation, properties, and relationships, see Hielscher et al. (2007) and Mainprice et al. (2015). We computed both indices using the MTEX toolbox v5.10.2 (Bachmann et al., 2010).

2.2.4. Modelling seismic properties

For seismic modelling, we used the MTEX toolbox v5.10.2 to compute seismic velocities and anisotropy using different averaging methods that considers the combined effects of elastic mineral properties and their arrangements within the rock (Mainprice et al., 2011). Specifically, we considered the Crystallographic Preferred Orientations (CPO), densities, and the relative volumetric contributions of major slate-forming mineral phases, which typically include quartz, muscovite, chlorite, and plagioclase, and other phases that constitute more than 2 % of the volume. The used single-crystal elastic properties and densities are listed in Table 2. Figures of anisotropy and seismic properties were plot using custom Python codes.

The specific procedure for estimating seismic velocities was as follows:

- 1. ODF estimation.** We estimated the Orientation Distribution Functions (ODFs) of all major mineral phases using the kernel density estimation method, as outlined by Hielscher and Schaeben (2008) and Hielscher (2013). The optimal kernel size was determined using the *De La Vallée Poussin* method recommended for ODF determination (Hielscher, 2013; Mainprice et al., 2011, 2015). The ODF was computed on a $\sim 1^\circ$ resolution grid (20,809 orientations), using one average orientation per grain, weighted by sectional area. This approach reduces the impact of low indexing rates in phyllosilicates (e.g., in PBT, RIM, BRA, and RVS; see Table 3) and minimizes potential bias due to orientation-dependent indexing. The number of independent grain orientations used for reconstruction typically exceeds 1000—and in some cases, 30,000—except for the BRA sample (Table 3). These large datasets and the adopted protocol ensure robust ODF reconstruction (cf. Bozzolo et al., 2007; Hielscher, 2013; Wagner et al., 1998).
- 2. ODF-weighted mineral elastic tensors.** The elastic tensor at room conditions of each mineral phase was adjusted to account for the preferred orientation of its grains represented by the ODF. The VRH or Hill's (Hill, 1952) and the geometric mean (Mainprice and Humbert, 1994) averaging methods were used.
- 3. Rock elastic tensor and density estimation.** The elastic tensor of the entire rock was then calculated by combining the ODF-weighted elastic tensors of each major mineral phase and its volumetric contribution normalised to 100 %. This step employed both the geometric and VRH (Hill's) averages. The overall rock density was calculated based on the densities of the individual minerals at room conditions (Table 2) and their corresponding volume fractions. Although the use of the Hill's average has no theoretical basis for being more appropriate than any other value within the Voigt and Reuss bounds, we use it here because it tends to give values close to experimental results (e.g. Hill, 1952; Mainprice and Humbert, 1994), which makes its use practical. Conversely, Cholach and Schmitt (2006) found that for phyllosilicate-rich rocks the geometric mean can give values for the non-diagonal components of the elastic tensor markedly different from the VRH average, even outside the Voigt and

Reuss limits. We provide the Voigt and Reuss bounds and a comparison between the two approaches and in the Supplementary Material (Table S3 and Fig. S1).

- 4. Seismic properties.** We estimated phase velocities as a function of propagation direction from the calculated elastic tensors using the Christoffel equation and rock density. All reported values and figures are based on tensors derived from the geometric mean. Following Naus-Thijssen et al. (2011b) and Wenk et al. (2022), we neglect grain shape effects. Because the elastic constants were measured at room conditions, the calculated seismic properties reflect the intrinsic properties of nonporous crack-free aggregates at room pressure.

Transversal and axial seismic anisotropy was calculated using the expression:

$$\text{Seismic Anisotropy (\%)} = 100 \times \frac{(V_{\max} - V_{\min})}{(V_{\max} + V_{\min})/2}$$

For the shear wave splitting (SWS), which measures the velocity difference between the fast and slow shear waves that occurs when a polarised shear wave enters an anisotropic medium, we used the expression:

$$\text{Polarization Anisotropy (\%)} = 100 \times \frac{(Vs1_i - Vs2_i)}{(Vs1_i + Vs2_i)/2}$$

where the subscript i refers to the fast ($Vs1$) and slow ($Vs2$) shear wave velocities at a specific propagation direction.

We also compared the calculated velocity models using the Christoffel equation, which account for the full complexity of the crystallographic texture and has a triclinic symmetry, with simpler models that assume higher symmetries. This comparison helps in assessing the predictive power of the simpler models. For this, we performed calculations to analyse the elastic tensor of slates under different symmetry assumptions, e.g. using tensor decomposition (Browaeys and Chevrot, 2004) and transverse isotropy parametrizations (Anderson, 1961; Thomsen, 1986) using custom Python codes available at <https://github.com/marcoalopez/PyRockWave>. To characterize the anisotropy of the tensor, we used Universal Elastic Anisotropy (UEA) (Ranganathan and Ostoja-Starzewski, 2008), the Kube's (log-Euclidean) anisotropy index (KAI) (Kube, 2016), and the percentage of the anisotropic component estimated by the decomposition method of Browaeys and Chevrot (2004). In all cases, we present crystallographic orientation and seismic properties as viewed normal to the foliation (XY plane) to facilitate visualization of azimuthal anisotropy, where present.

2.2.5. Correlations between rock fabric, CPO intensity and seismic properties

The seismic properties of slates, particularly their anisotropy, are strongly influenced by the typical arrangement of major forming minerals, with a pronounced impact related to the phyllosilicate fraction and the strength of the phyllosilicate Crystallographic Preferred Orientations (CPO). To assess how the volumetric content and the CPO of phyllosilicates affects the seismic properties of slates, we employ two proxies: the normalised J-index, as proposed in Cárdenes et al. (2021), and the normalised S-index, which is based on the orientation distribution function (ODF) entropy. Both methods integrate the ODF intensity of the different phyllosilicates weighted according to their volumetric fraction. This weighting considers only the phyllosilicates and is subsequently normalised by the total phyllosilicate fraction in the slate as follows

$$S_{\text{norm}} = S_{\text{phyllosilicates}} \times \varphi_{\text{phyllosilicate}}$$

$$S_{\text{phyllosilicates}} = (S_{\text{Ms}}\varphi_{\text{Ms}} + S_{\text{Chl}}\varphi_{\text{Chl}} + \dots)$$

where φ represent area fractions and, by assumption, volume fractions.

3. Results

3.1. Mineral content and microstructure

The set of slates/phyllites examined shows a wide variation in phyllosilicate fraction, ranging from 44.6 to 73.0 % by volume (Fig. 1), and *Chl* to *Ms* ratios, ranging from 0.33 to 0.81 (see Table S1 in the Supplementary Material). Among the other major phases considered, all samples contain quartz and, except for PBT, WA, and CA, feldspar. The PBT sample is unique in that it contains significant amounts of chloritoid, comprising 11.7 % of its composition (Fig. 1). Epidote is also present in small but significant fractions in two samples, the phyllite RVS and the quartzite ALT.

The microstructure of the studied slates is consistent with that of low-grade metamorphic rocks characterised by a slaty cleavage (see EBSD maps in Supplementary material). Planar minerals, such as muscovite and chlorite, are oriented and define the slaty cleavage. Non-planar minerals, such as quartz and feldspar, exhibit varying degrees of alignment with the slaty cleavage and shape fabrics. Secondary minerals (metamorphic overgrowths of phyllosilicates and quartz) can develop strongly elongated shapes parallel to the slaty cleavage. Strain shadows filled with quartz are a common occurrence. Rocks with a slightly higher metamorphic grade tend to exhibit less elongated crystal shapes. However, regardless of the degree of metamorphism and mineral elongation, as roofing slates all samples are characterised by exceptional cleavage development and strong mineral orientation with the slate cleavage.

3.2. Crystallographic preferred orientation

Crystallographic Preferred Orientation (CPO) patterns in phyllosilicates can be categorized into two types: those where the phyllosilicate c-axis forms a point maximum normal to the slaty cleavage, and those where the c-axis forms a girdle or semi-girdle normal to the intersection lineation, with the point maximum normal to the slaty cleavage (Fig. 2). In slates, the c-axis pole figures of muscovite and chlorite show a wide

variation in intensity, from 10 to exceptionally high intensities of 80 multiples of a uniform distribution. The S-index ODF intensity (absolute) values vary from 0.25 (*Ms* in WA) to 3.2 (*Chl* in GXE), with the S-index averages being 1.5 for muscovite and 2.0 for chlorite (Table S2 in Supplementary material).

Chloritoid in the PBT slate shows a strong CPO, with the c-axis maxima oriented normal to the slaty cleavage, forming a semi-girdle normal to the intersection lineation (Fig. 2). Despite not being a phyllosilicate, we have included chloritoid in the phyllosilicate fraction due to its strong CPO and seismic anisotropy properties ($V_p = 22\%$, $V_s > 40\%$, $SWS = 46.5\%$), as these features closely mirror the CPO patterns and the pronounced anisotropic seismic features of phyllosilicates.

The silt fraction under consideration here is primarily composed of quartz and feldspar, exhibiting weak to almost random CPOs. The average J-index Orientation Distribution Function (ODF) intensity values are 1.26 for quartz and 1.12 for albite (see CPO patterns in Supplementary Material). Epidote, present in the RVS slate (2.1 %) and the ALT quartzite (2.5 %), developed a CPO, particularly in the slate, where the b-axis (fastest) reaches more than 6 multiples of a uniform distribution and aligns parallel to the intersection lineation.

3.3. Seismic speeds and anisotropy

3.3.1. Calculated P-wave speeds and anisotropy

Calculated P-wave velocities in slates vary from 5.4 to 6.0 km/s normal to the foliation and from 6.5 to 7.4 km/s within the foliation (Figs. 3 and 4). As expected, the faster velocities consistently occur within the foliation, typically parallel to the lineation, while the slower velocities occur normal to the foliation, except in the RIM slate where they are oblique (Figs. 3 and 4). Notably, the PBT sample displays faster minimum and maximum P-wave velocities than the others (Fig. 3). This difference is attributed to the presence of chloritoid (11.7 % in volume) with a strong crystallographic orientation in this sample. This mineral has faster P-wave velocities than phyllosilicates, and its fast direction, parallel to the a-axis, aligns within the foliation plane (Fig. 2). The mica-

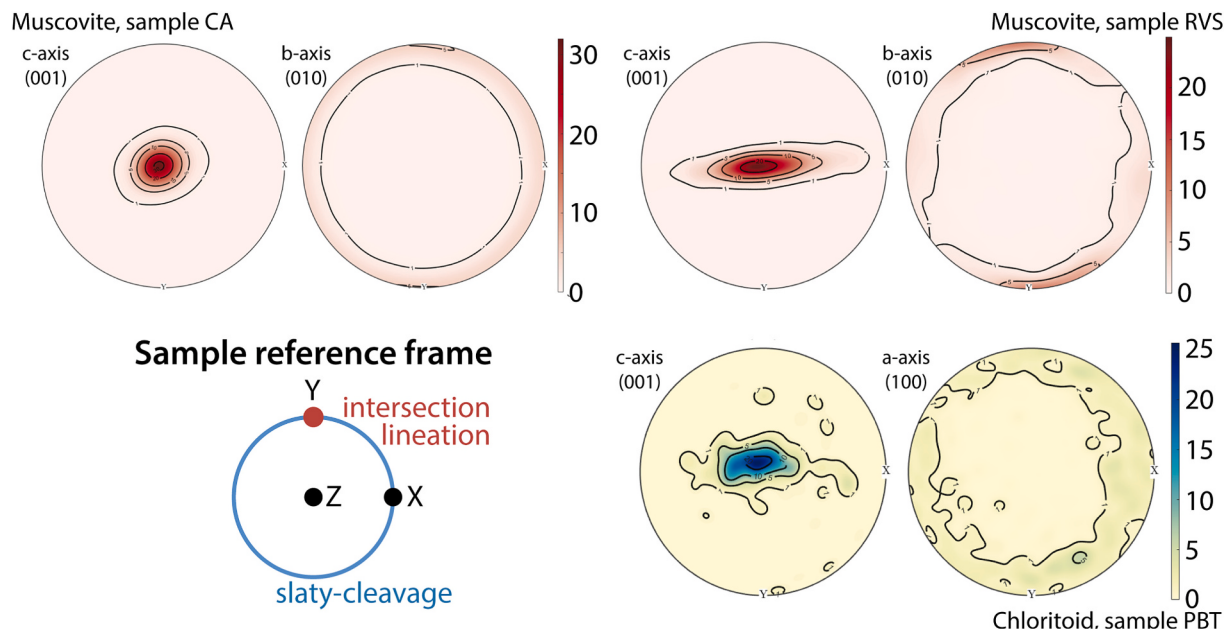


Fig. 2. Typical CPO patterns in the studied samples. Upper row: Typical phyllosilicate (muscovite and chlorite) CPOs in slates. On the left, the c-axis forms a point maximum normal to the foliation, and the b- and a-axes are oriented randomly within the foliation (samples ALT, ANL, BEI, BRA, CA, EUP, GXE, OSO, WA). On the right, the c-axis forms a semi-girdle with a point maximum normal to the foliation and spreads perpendicular to the intersection lineation. The a- and b-axes are oriented with the foliation, showing a complete girdle with a maximum parallel to the intersection lineation (samples RVS, PBT, RIM). Bottom row: On the left is the reference frame of the sample with respect to the pole figure. On the right, the chloritoid CPO pattern in the PBT sample showing a similarity with the phyllosilicate CPO patterns with the c-axis arranged normal to the foliation and the a- and b-axes oriented randomly within the foliation. Upper hemisphere equal-area projections, contours in multiples of a uniform distribution. All CPO pole figures are provided in the Supplementary Material.

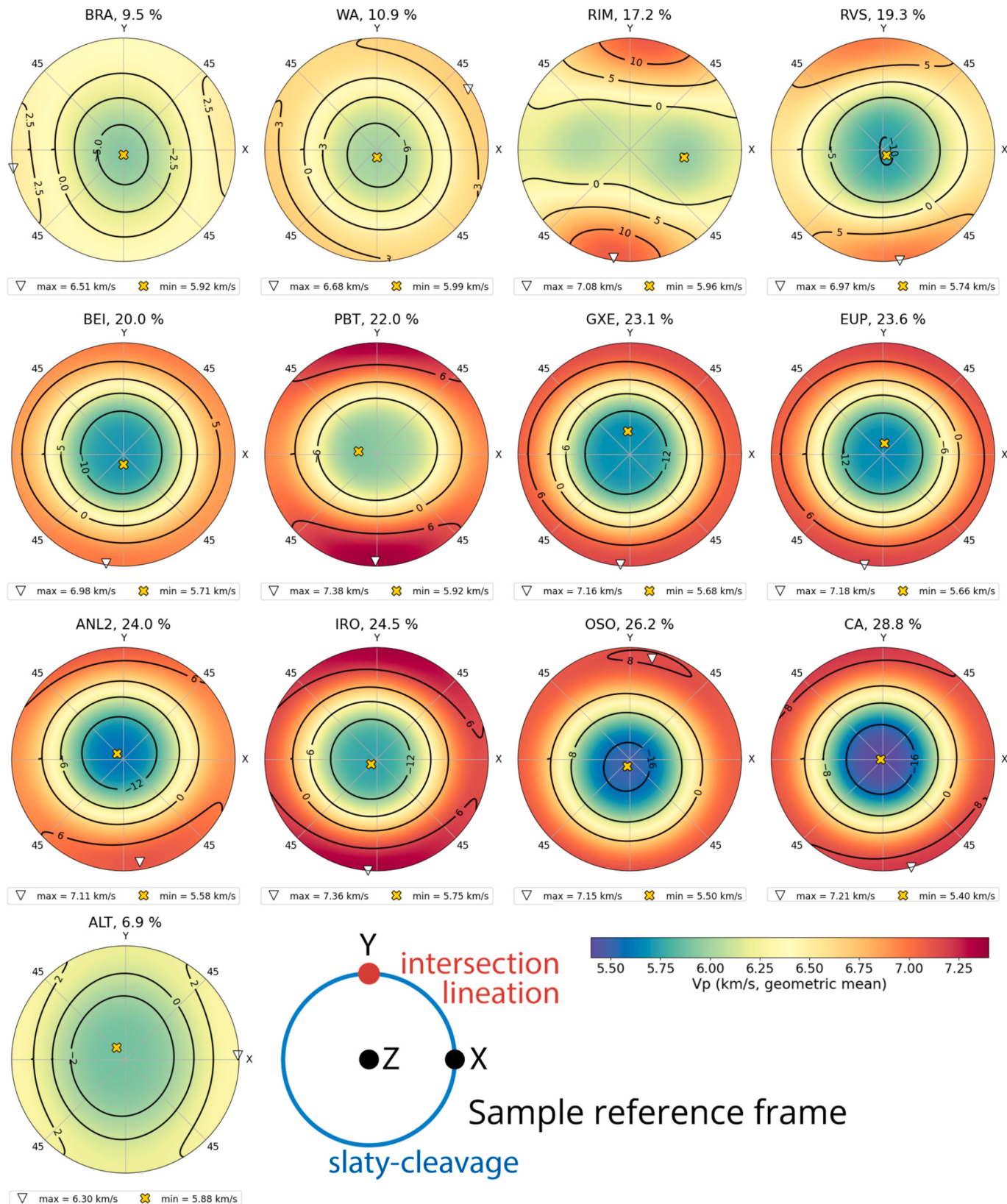


Fig. 3. Calculated P-wave velocities as a function of orientation illustrated in pole figures (upper hemisphere), where the major circle represents the foliation (slaty cleavage) plane. The colour scale representing absolute velocities is consistent across all figures. Contour lines represent percentages above (positive) and below (negative) the median velocity. The sample reference and its maximum anisotropy in percent are indicated above each pole figure. The orientations of the maximum and minimum P-wave velocities are marked by white triangles and yellow crosses, respectively. (For interpretation of the references to colour in this figure legend, the reader is referred to the web version of this article.)

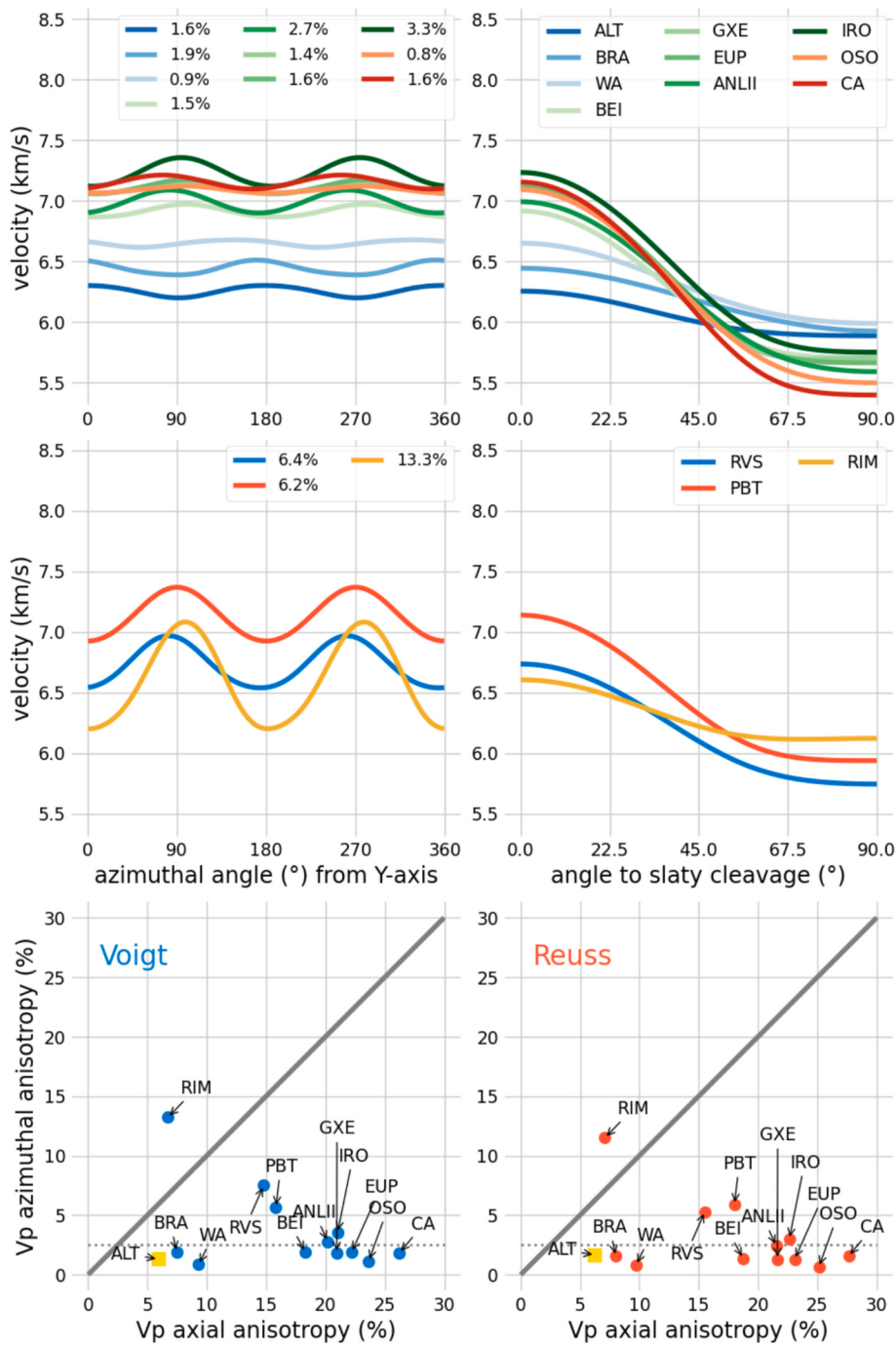


Fig. 4. Calculated azimuthal and axial P-wave anisotropy profiles for the different samples. The top row shows several slates and the quartzite ALT, all exhibiting approximately transverse isotropy with low azimuthal anisotropies (<3.3 %). The middle row displays slates with notable azimuthal anisotropies ranging from 6.4 to 13.3 %. The RIM slate shows higher azimuthal than axial anisotropy indicating a clear orthorhombic symmetry. The PBT slate (in red), the only slate with significant amounts of chloritoid, stands out by its higher P-wave velocities parallel to the intersection lineation. Bottom row, azimuthal versus axial anisotropy for P-wave velocities using Voigt and Reuss bounds. Blue and red dots denote slates and the yellow square denotes the micaceous quartzite. The dotted line marks a 3 % azimuthal anisotropy. Most single-foliated slates have intrinsic transverse anisotropies below 3 % and a wide range of axial anisotropy, from 6 to 28 %. Transverse profiles represent average azimuthal velocity with respect to angle to foliation. (For interpretation of the references to colour in this figure legend, the reader is referred to the web version of this article.)

bearing quartzite shows slower P-wave velocities than the slates (Figs. 3 and 4).

P-wave anisotropies in slates vary widely, ranging from 9.5 to 28.8 % (Figs. 3 and 4). The quartzite shows moderate anisotropies (6.9 %), while the serpentine displays values similar to those of slates with orthorhombic symmetries (e.g., RIM, RVS). In terms of anisotropy symmetry, most slates are in practice transversely isotropic (i.e.,

hexagonal-like symmetry), with azimuthal anisotropies varying between 0.8 and 3.3 % (Fig. 4). Conversely, three slates (RVS, PBT, and RIM) show significant azimuthal anisotropies, ranging from 6.2 to 13.3 % (Fig. 4), displaying orthorhombic-like symmetries for P-waves (Fig. 3). The RIM sample is the only slate case where the azimuthal anisotropy exceeds the axial one, at 7.6 versus 13.3 % (Fig. 4).

3.3.2. Calculated S-wave speeds and anisotropy

Calculated S1-wave (fast) velocities in slates vary from 3.3 to 3.8 km/s normal to the foliation and from 4.0 to 4.5 km/s within the foliation, polarising parallel to the foliation plane in directions containing or disposed at a low angle ($\sim 45^\circ$) to the slaty-cleavage (Fig. 5). The faster velocities are consistently contained within the foliation, although unlike P-waves they do not align with the slate lineation. The slower S1 velocities lay perfectly normal to the foliation. The micaceous quartzite displays S1-wave velocities at the range limits identified in the slates (Fig. 5). In the slates, the mean (isotropic) V_p/V_s ratios vary between 1.64 and 1.71, with mica-bearing quartzite showing a significant difference with a ratio of 1.54 (see Table S4 in the Supplementary Material).

Regarding seismic anisotropy, S-wave anisotropies in slates vary widely, ranging from 5.6 to 29.9 % for the fast S1-wave (Fig. 5) and between 2.1 and 15.6 % for the slow S2-wave (see Supplementary material). In contrast, the micaceous quartzite shows a lower S1-wave anisotropy (1.6 %) than the slates. In terms of anisotropy symmetry, all slates except the RIM sample are effectively transversely isotropic (i.e., hexagonal-like) (Fig. 6).

3.3.3. Calculated polarization anisotropy: shear-wave splitting

In slates, the calculated polarization anisotropy (shear-wave splitting) varies from almost negligible values, typically at 45 degrees to the slaty cleavage, to maximum polarization values within the foliation plane, ranging widely from 6.7 to 30.2 % (Fig. 6). Quartzite exhibit similar polarization anisotropy pattern to slates, with maximum anisotropy for quartzite at the lower end of the range established for slates (6.7 %). The polarization anisotropy for normal and near-normal to the foliation incidences is very small or negligible for most cases, in agreement with a transverse isotropic medium. Only the slate RIM have measurable near-vertical SWS values, close to 10 %. This observation aligns with the assumption that when shear-wave splitting is observed at near-vertical incidences, there must be corresponding azimuthal effects on P-wave velocities (Thomsen and Anderson, 2015).

3.3.4. Calculated elastic constants: variability and tensor decomposition

The complete elastic constants calculated using the Voigt, Reuss, Hill and geometric mean approaches for all samples are given in Table S3 in the Supplementary Material. In Table 4, we provide as reference values the five independent elastic constants calculated for slates with transverse isotropy seismic properties estimated by tensor decomposition into its isotropic and hexagonal components (i.e. ignoring all the parts with symmetries lower than hexagonal). The anisotropic fraction (in percent) of the decomposed tensor and two universal anisotropy indexes (UAI, KAI), see section 2.2.4 for details, are also given.

The anisotropic part of the calculated elastic tensors after decomposition varies from 6.4 % (BRA) to 21.0 % (CA) in slates (Table 4) (see Table S5). Analysis of the symmetry of the anisotropic part of the tensor in slates shows that the majority corresponds to hexagonal symmetry ($>74\%$), with most having a limited ($<10\%$) orthorhombic component (Fig. 7). Outside this trend are the PBT, RVS, BRA and RIM slates, being the latter the only one where the orthorhombic component dominates, although all other components are present and balanced (Fig. 7).

Regarding the strength of the correlation between the different elastic components in the transversely isotropic slates, linear correlations are strong between the diagonal components, especially between C66 and C11 (Pearson's coefficient of 0.96), C66 and C44 (-0.93), C44 and C66 (-0.93), C33 and C44 (0.83), and C66 and C33 (-0.83) (Fig. 8). In contrast, the correlation between C11 and C33 is weaker (-0.74), and the off-diagonal component C13 lacks correlation with the diagonal components (Fig. 8).

4. Discussion

Most slate samples studied here display the typical quasi-transverse

isotropy. All but three show azimuthal P-wave anisotropies ranging from 0.8 to 3.3 % (Fig. 4). Axial anisotropy varies widely: P-wave anisotropy ranges from 9.5 % to 28.8 %, V_s from 5.6 % to 29.9 %, and polarization anisotropy (SWS) along foliation from 6.7 % to 30.2 %, decreasing to negligible values normal to foliation. Average (isotropic) velocities fall between 6.3 and 6.5 km/s for P-waves, 3.8–3.9 km/s for S-waves, with V_p/V_s ratios between 1.64 and 1.71.

Our calculated anisotropy values are comparable to those measured experimentally by Guo et al. (2014) at 600 MPa, who reported 13–16 % P-wave anisotropy, ~ 18 % S-wave anisotropy, and 7–12 % polarization anisotropy parallel to foliation, with negligible values perpendicular to it. Our dataset, however, is larger and includes slates with both weaker and stronger CPOs, resulting in a broader range—especially at the upper end. Average P-wave velocities align with Guo et al.'s (6.3 km/s), but our S-wave velocities (3.8–3.9 km/s) are slightly higher than their 3.62 km/s, leading to marginally lower V_p/V_s ratios. This difference likely reflects mineralogical differences: our samples contain chlorite, which has higher isotropic V_s (4.25 km/s) than the biotite (3.4 km/s) present in Guo et al.'s slates. Additionally, our modelled P- and S-wave velocities along foliation are consistently ~ 5 –10 % higher than those measured at room conditions on the same samples by Cárdenes et al. (2021) (Fig. S4, Supplementary Material). The agreement between our results and those obtained experimentally at pressures above 150 MPa supports the internal consistency and physical plausibility of our modelling.

We hypothesize that slates with higher azimuthal anisotropies (RIM, PBT, and RVS), falling between 6.4 and 13.3 % (cf. Fig. 4), that exhibits orthorhombic or minor symmetry components may be attributed to incipient crenulation of the slaty cleavage. This interpretation is supported by the alignment of the maximum axial P-wave anisotropy parallel to the intersection lineation and by the development phyllosilicate c-axis semi-girdles normal to the lineation observed in such rocks (Fig. 2). Similar phenomena, characterised by c-axis semi-girdles normal to the lineation, have been previously documented in single-foliated crenulated slates (Naus-Thijssen et al., 2011a; Wenk et al., 2020). Interestingly, these three samples, along with BRA, show low EBSD indexing of the phyllosilicate fraction (< 20 %, cf. Table 3), which hinders reliable microstructural reconstruction and may bias ODF calculations. Their deviation from typical transverse isotropy may partly reflect this issue. We therefore exclude the RIM, PBT, and RVS samples from all subsequent analyses.

When comparing the seismic features of slates to those of the reference micaceous quartzite, several distinctions and similarities emerge. Both the P- and S-wave average (isotropic) velocities of the quartzite fall within the range observed for the slates. However, the quartzite displays significantly reduced P-wave and S1-wave anisotropies, especially for S1 (1.6 %), only attributed to its lower phyllosilicate content. Moreover, a substantial dissimilarity lies in the isotropic V_p/V_s ratio, which is notably lower in the mica-bearing quartzite (1.57) compared to the range observed in the slates (1.64–1.71).

In terms of comparison with shales, the linear correlations found in transversely isotropic slates between the different elastic constants forming the diagonal of the elastic tensor mirror those found in shales (Horne, 2013). However, our dataset indicates a lack of linear relationship between the off-diagonal component C13 and all the others. These correlations suggest that it would be theoretically feasible to estimate the five elastic constants needed to fully define hexagonal symmetry from just two measurements: one diagonal component, optimally C66, and the off-diagonal component C13. The lack of correlation between the off-diagonal component C13 and the other components makes the model proposed by Sayers and den Boer (2020) for shale, where the remaining constants are calculated only from the C33, inappropriate for slate at conditions where intrinsic factors govern the elastic response. These findings underline the optimal strategy for modelling the limits of the intrinsic seismic properties of single-foliated slates, which involves taking the average and typical variance values of the C66 and C13 elastic constants given in Table 4 and extrapolating the others from these.

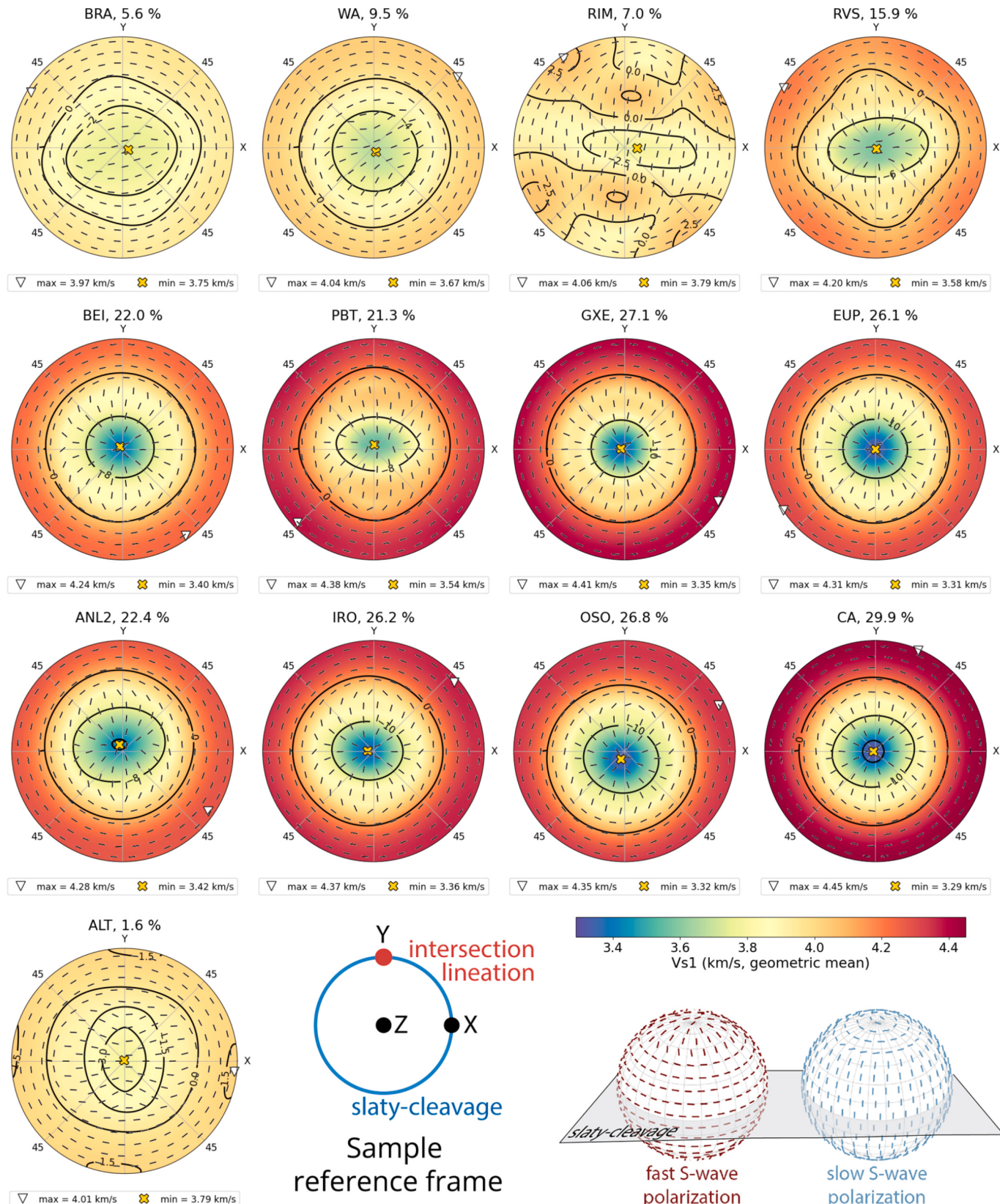


Fig. 5. Calculated fast S-wave velocities as a function of orientation illustrated in pole figures, where the major circle represents the foliation plane. The colour scale representing absolute velocities is consistent across all figures. Contour lines represent percentages above (positive) and below (negative) the median velocity. The sample reference and its maximum anisotropy in percent are indicated above each pole figure. The orientations of the maximum and minimum fast S-wave velocities are marked by white triangles and yellow crosses, respectively. Bottom right corner: 3D visualization of the typical polarization of fast and slow S-waves in (quasi-) transversely isotropic slates. Pole figures of fast and slow S-wave velocities with polarizations are provided in the Supplementary Material. (For interpretation of the references to colour in this figure legend, the reader is referred to the web version of this article.)

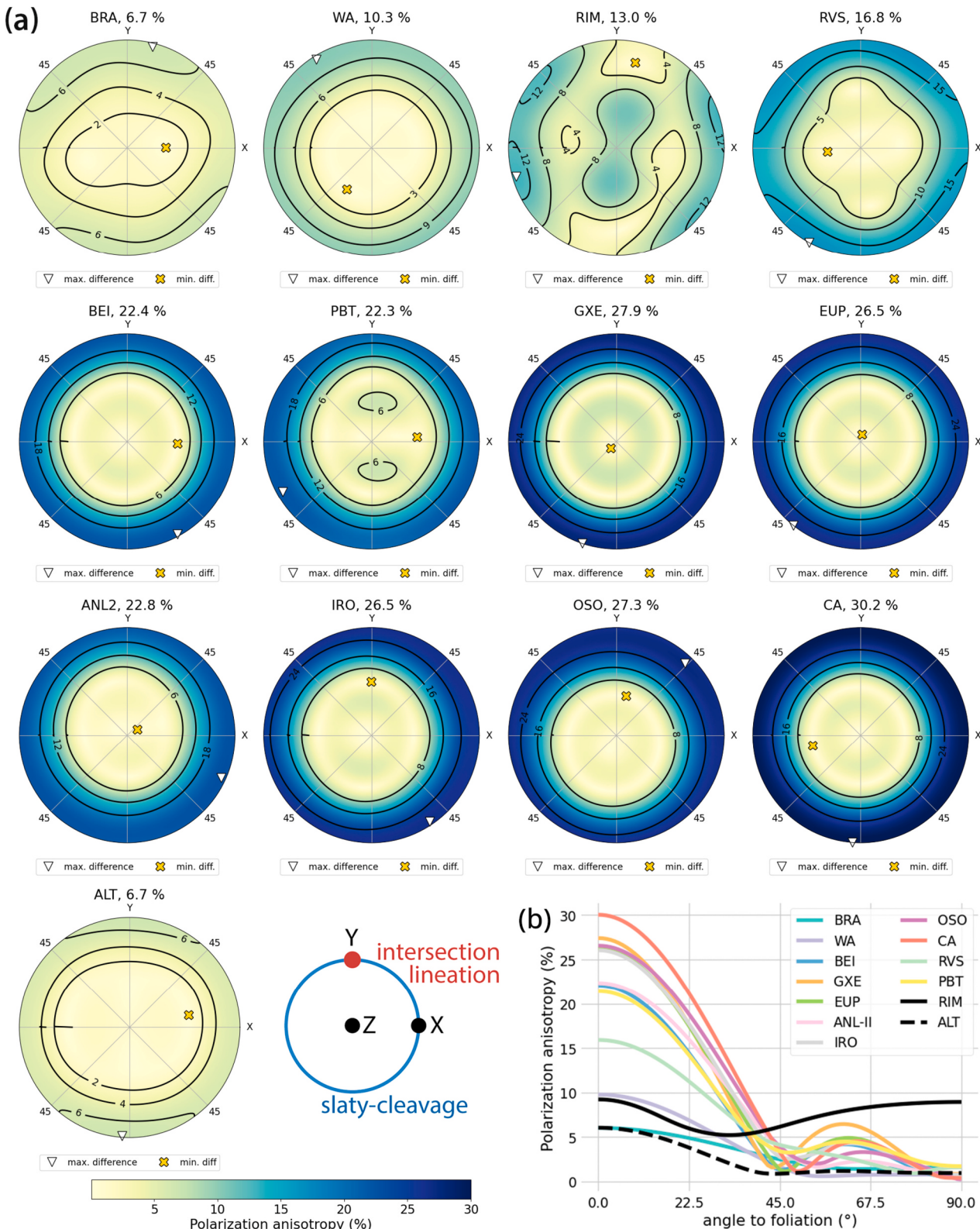


Fig. 6. (a) Calculated polarization anisotropy (shear-wave splitting) in percent as a function of orientation illustrated in pole figures, where the major circle represents the foliation plane. The colour scale is consistent across all figures. The reference of the sample and its maximum polarization anisotropy are shown above each pole figure. White triangles and yellow crosses, respectively, indicate the orientations of the maximum and minimum polarization anisotropy. Note that the maximum polarization always lies within or very close to the foliation plane. (b) Polarization anisotropy axial profiles. Minimum polarizations are at $\sim 45\text{--}47^{\circ}$ or normal to the foliation, except for the RIM slate (black solid line). (For interpretation of the references to colour in this figure legend, the reader is referred to the web version of this article.)

Table 4

Reference values for the five independent elastic constants and densities calculated for transversely isotropic slates used by the Anderson parametrization and various anisotropy elastic tensor indexes. CV (%) denotes coefficient of variation (variance respect to the mean in percentage) at 1-sigma level.

Sample	C ₁₁	C ₃₃	C ₄₄	C ₆₆	C ₁₃	density (g/cm ₃)	anisotropy (%)	UAI	KAI
BRA	112.6	95.3	37.5	42.3	27.2	2.712	6.4	0.031	0.013
WA	121.8	98.8	36.9	44.8	30.1	2.753	8.5	0.062	0.025
BEI	130.0	88.5	31.3	48.7	25.9	2.716	16.0	0.277	0.111
GXE	137.8	88.8	30.5	52.9	23.2	2.726	18.8	0.417	0.165
EUP	138.2	87.6	29.8	50.6	28.5	2.729	18.2	0.399	0.158
ANL-II	134.9	86.3	32.4	50.3	28.5	2.759	16.7	0.305	0.121
IRO	142.8	90.7	31.1	51.8	31.3	2.737	17.8	0.377	0.150
OSO	137.9	83.0	30.7	51.5	27.4	2.745	18.8	0.415	0.164
CA	141.0	80.3	29.8	54.6	23.3	2.754	21.0	0.545	0.213
mean	133.0	88.8	32.2	49.7	27.3				
CV (%)	7.5	6.4	9.1	7.8	10.1				

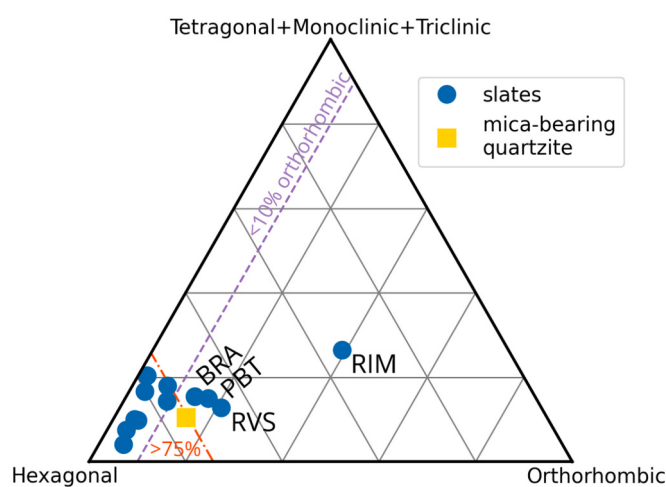


Fig. 7. Decomposition analysis of the calculated elastic tensors (geometric mean) illustrating the proportion of hexagonal to orthorhombic to lower symmetry components for all the samples. The purple dashed line indicates the <10 % orthorhombic symmetry threshold, while the orange dash-dotted line indicates the >75 % hexagonal symmetry threshold. Slates outside these thresholds are labelled. (For interpretation of the references to colour in this figure legend, the reader is referred to the web version of this article.)

4.1. Are transverse isotropy models good enough for predicting anisotropy in single-foliated slates?

Using the calculated elastic tensors, we tested the predictive power of three different transverse isotropy (polar) parameterizations for single-foliated slates in terms of anisotropy. For this analysis, we ignored the micaceous quartzite (ALT) and the slates RVS, PBT, and RIM, as they all have significant non-hexagonal components.

Comparing the anisotropy values predicted by the different polar parametrizations with those estimated with the Christoffel-based approach (Table 5), we found that the weak polar anisotropy (Thomson) model is the least suitable of the three, with errors in excess of 10 % in most cases because of the strong axial anisotropy of single-foliated slates. The Anderson parametrization (Anderson, 1961) gives better predictions, particularly when using along with the decomposed hexagonal elastic tensor instead of the values from the full (21 components) calculated tensor. The estimation of axial anisotropy by the tensor decomposition plus Anderson parametrization yield practically identical results for P-waves (errors ~0.2 %), very good estimates for polarization anisotropy (average of 1.1 %), and slightly worse for S-waves, with an average of 2.8 % although it exceeds 15 % in one case (see sample BRA in Table 5). Interestingly, the BRA slate has the lowest hexagonal component of all the slates used, <74 %, which is the threshold used in Fig. 7, and suffer from EBSD indexation problems in phyllosilicates. We

therefore conclude that the Anderson parametrization together with the decomposition of the geometric mean (or VRH) tensor into its hexagonal part is the best predictive model of the three polar parameterizations for single-foliated slates.

In view of these results, we propose that the use of the Anderson parameterization should be sufficient for the modelling and averaging of intrinsic seismic properties in transverse isotropy rocks such as single-foliated slates and shales. This model should be particularly advantageous when using deep and machine learning strategies, as the Anderson parameterization is much faster than the Christoffel-based procedure. Therefore, for modelling single-foliated slates, we provide in Table 4 a set of five reference elastic constants with their typical variance calculated from the decomposition of the tensor into its isotropic + hexagonal parts.

4.2. Are phyllosilicate content and ODF intensity good predictors of seismic anisotropy and vice versa?

The plots depicted in Fig. 9 reveal a robust positive linear correlation between the S-norm proxy proposed here and both the maximum Vp, Vs1 and polarization anisotropy in the slates. Linear models of the form $y = mx$, where y represents the S-norm, x denotes the anisotropy, and m symbolized the slope, explain more than 0.96 of the data in all cases. We limited b (i.e. the intersection) to 0 since, theoretically, a zero S-norm value (indicating no preferred phyllosilicate orientation) should yield a null anisotropy value when extrinsic factors are ignored. Accordingly, the Vp, Vs, and polarization anisotropy of the slates can be predicted from the proxy with a confidence interval at the 2-sigma level of ±12 % in axial anisotropy and ± 9.5 % in polarization anisotropy. While these relationships similarly apply to the J-norm proxy, the predictive power of the S-norm is superior (refer to Supplementary Material), prompting our focus solely on this proxy.

Considering only the phyllosilicate fraction or the ODF intensity, we observed that the relationship between seismic anisotropy and phyllosilicate fraction alone is weak, whereas a stronger positive correlation exists between the phyllosilicate ODF intensity and anisotropy. In any case, the correlation between these variables alone is not as robust as the correlation with the S-norm proxy, which accounts for both. This suggests that, of the intrinsic factors, the intensity of the crystallographic orientation of the phyllosilicates has the strongest influence on the seismic anisotropy in slates playing the phyllosilicate/silt fraction a secondary role.

Reverse prediction, i.e. using axial or polarization anisotropy values measured in geophysical surveys to estimate phyllosilicate fraction or CPO intensity, is theoretically possible. However, as the S-norm proxy involves two independent variables, the phyllosilicate ODF strength and the phyllosilicate/silt fraction, the calculation gets more complicated as it requires the assumption of a characteristic phyllosilicate ODF intensity or phyllosilicate fraction due to the additional degree of freedom (Fig. 9b). The plots in Fig. 9b show that in some cases it is possible to

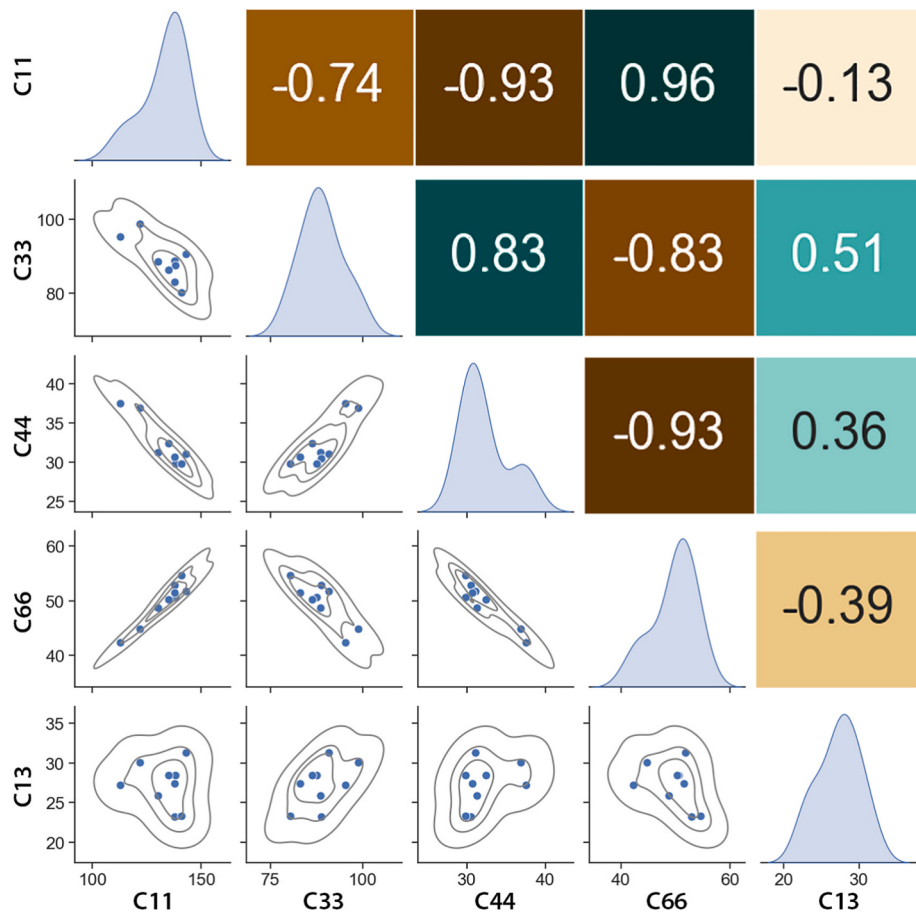


Fig. 8. Pair plot (bottom left corner) showing the correlations between the different independent elastic constants in transversely isotropic slates, accompanied by an annotated heat map (top right corner) with corresponding standard Pearson linear correlation coefficients.

Table 5

Percentage error in the estimation of the maximum axial and polarization (SWS) anisotropy compared to the estimation using the Christoffel-based approach. Positive values indicate overestimation and negative values underestimation. Mean values are given as absolute errors.

Sample	Vp (%)	Vs1 (%)	SWS (%)		Vp (%)	Vs1 (%)	SWS (%)		Vp (%)	Vs1 (%)	SWS (%)
	Thomsen model				Anderson model				decomposition + Anderson model		
BRA	16.8	29.5	11.7		11.6	25.4	8.3		-0.1	15.4	0.0
WA	7.4	11.1	6.1		2.0	5.9	1.0		0.0	4.0	-1.0
BEI	5.2	12.6	10.9		-3.6	1.5	0.0		0.0	1.1	-0.5
GXE	7.0	16.6	14.6		-3.2	2.7	0.7		0.0	1.5	-0.4
EUP	7.2	14.9	13.3		-3.3	1.7	0.4		-0.1	1.1	-0.4
ANLii	4.0	9.8	6.7		-5.8	-0.8	-3.6		-0.1	1.2	-1.8
IRO	1.7	12.8	10.0		-7.9	0.2	-2.3		-1.2	-0.3	-2.7
OSO	10.5	11.9	8.7		-1.6	-0.7	-3.4		-0.3	-0.2	-3.0
CA	10.5	16.1	15.3		-2.5	1.3	0.7		0.0	0.6	0.0
mean	7.8	15.0	10.8		4.6	4.5	2.3		0.2	2.8	1.1

derive practical information about the phyllosilicate fraction range from a measurement of axial or polarization anisotropy without making assumptions about the CPO phyllosilicate intensity just by assuming a rough range of values. For example, if we measure seismic anisotropies equal to or greater than 24 %, as is the case for the CA and OSO samples, we can infer from Fig. 9b that the slates contain phyllosilicate fractions greater than ~50 %, regardless of the CPO intensity. Note that this inference assumes that the ranges of CPO phyllosilicate intensity lie within the range shown in Fig. 9b (S-index < 2.7) and that extrinsic factors are not significant.

4.3. Model limitations

There are several limitations to the models presented here. Firstly, to establish the relationships we have ignored the effect of extrinsic factors such as the effect of porosity, shape fabrics or the interplatelet medium elastic properties. It is known from V_p versus pressure curves that extrinsic factors are non-negligible in slates at confining pressures below 150 MPa (~6 km) (e.g. Cholach et al., 2005; Guo et al., 2014). It is also known that in the case of slates, extrinsic factors cause an increase in aggregate anisotropy, indeed at very low pressures and under dry conditions some of the slate modelled here have anisotropies up to 66 % in V_p (Cárdenes et al., 2021), see also fig. S4 in Supplementary Material. Thus, for slates at shallower than ~5–6 km depth in the crust, it would

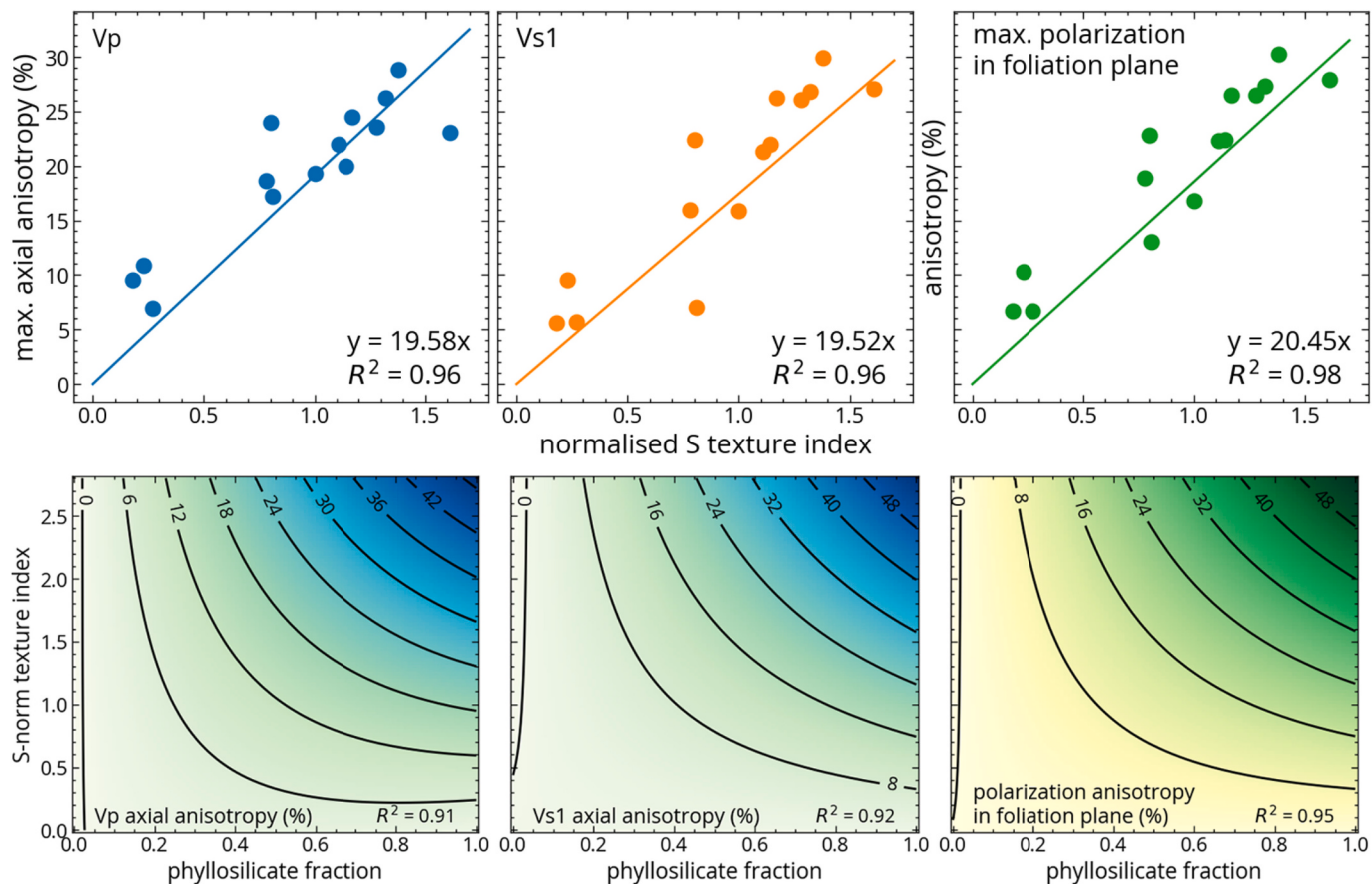


Fig. 9. Anisotropy model for transversely isotropic single-foliated slates. Upper row: Linear correlation between the S-norm proxy introduced here and different types of axial anisotropy including Vp, Vs1, and polarization (shear-wave splitting) anisotropies. Bottom row: Phyllosilicate fraction vs. phyllosilicate ODF texture strength (S-index) as a function of Vp, Vs1, and polarization anisotropies in percentage. The correlation was estimated by fitting a polynomial equation using a least squares fitting algorithm (see Supplementary Material for details).

be necessary to account for these extrinsic factors to correct the anisotropy estimates. In any case, even with this limitation the model is fully valid to determine a minimum anisotropy and maximum absolute wave speeds based on intrinsic (ODF strength and phyllosilicate content) properties.

Another limitation, common to all studies of slate seismic properties, is the lack of experimental data at pressures and temperatures relevant to the middle crust. To date, only Guo et al. (2014) have provided measurements up to 600 MPa although at room temperature. The same applies to phyllosilicates, for which pressure and temperature derivatives of elastic constants are largely unavailable. Further experimental work is needed to refine and validate numerical models.

Another limiting extrinsic factor, acting on a much larger scale than the previous ones, is the possible presence of layering finer than the seismic wavelength used. This factor is important because layering is common in sedimentary basins and its seismic effects are independent of the confining pressure acting on rocks. Simplifying, layering (parallel to the Earth's surface) will increase the axial anisotropy of the rock, as the most common sedimentary rocks alternating with slates, such as sandstones or limestones, have lower seismic velocities and will slow down wave velocities normal to layering. Similarly, the development of tectonic banding, differentiation between quartz-rich and phyllosilicate-rich bands, is expected to enhance anisotropic behaviour. In any case, the seismic effect and magnitude produced by fine layering in slate belts, and all the variables that characterize layering, need to be further studied. It is also noteworthy that in some cases the slaty cleavage in slate belts is expected to arrange at a high angle to the Earth's surface.

The last limiting factor relates to the fact that the samples used here

are essentially single-foliated, and slates tend to develop crenulations or kink bands in slate belts affected by orogenic processes. Such microstructures will change the symmetry of the elastic tensor away from a hexagonal symmetry towards orthorhombic or lower symmetries, in a similar way to the RIM sample studied here or those studied by Naus-Thijssen et al. (2011a). The effect of these microstructures in the model is a topic that requires further investigation. Interestingly, the slightly orthorhombic (RVS and PBT) and more orthorhombic (RIM) samples studied here fit the model estimating maximum anisotropies, suggesting that the S-norm proxy does not fully lose its predictive power in such cases.

5. Conclusions and future prospective

We have used a comprehensive set of high-quality single-foliated slates and large-coverage EBSD mapping to calculate their typical seismic properties (absolute velocities, anisotropy, and correlations between elastic constants) using the geometric mean averaging method. With these data, we have investigated which transverse isotropy (polar) models give the best predictions and whether it is possible to predict the intrinsic maximum anisotropy of these rocks from a single proxy.

We found that axial and polarization anisotropy can be reliably estimated in single-foliated slates with an error of ~10 % based on a single proxy, named the S-norm, which accounts for the ODF strength and the volumetric fraction of phyllosilicates and chloritoid in slates. We have also found that a polar parameterization based on a combination of elastic tensor decomposition and the Anderson equations gives seismic anisotropy predictions similar to the Christoffel equation with errors

generally better than 2.8 % (0.2 % for Vp). These models should be practical for investigating slate belts at depths greater than 6 km (~150 MPa), but also at shallower depths as they allow the minimum expected seismic anisotropy to be calculated from their intrinsic properties.

The main limitation of the models proposed here is that they only consider intrinsic factors, and under certain circumstances, it will be necessary to include corrections for extrinsic factors (e.g., oriented fractures/porosity and layering) and/or consider the role and degree of crenulation or kink-bands development.

CRediT authorship contribution statement

Marco A. Lopez-Sánchez: Writing – review & editing, Writing – original draft, Visualization, Validation, Software, Methodology, Formal analysis, Data curation, Conceptualization. **Víctor Cárdenes:** Writing – review & editing, Visualization, Resources, Investigation, Funding acquisition, Data curation. **Fabrice Barou:** Writing – review & editing, Methodology. **Sergio Llana-Fúnez:** Writing – review & editing, Resources, Investigation.

Declaration of competing interest

The authors declare that they have no known competing financial interests or personal relationships that could have appeared to influence the work reported in this paper.

Acknowledgements

This work was supported by the Government of the Principality of Asturias, the European Union (Marie-Curie COFUND) and the Foundation for the Promotion of Applied Scientific Research and Technology in Asturias (FICYT) (Spain) (Grant numbers: SV-PA-21-AYUD/2021/57163, PA-18-ACB17-11) under the “*Plan de Ciencia, Tecnología e Innovación 2018–2022*” of Asturias (PCTI-Asturias). We thank Luiz F.G. Morales and two anonymous reviewers for their insightful suggestions, which improved the clarity and quality of the manuscript. We are also grateful to Doug R. Schmitt for his comments on an earlier draft and to Samuel Angiboust for editorial guidance.

Appendix A. Supplementary data

Supplementary data to this article can be found online at <https://doi.org/10.1016/j.tecto.2025.230765>.

Data availability

The data and codes necessary to reproduce the results of this article are attached to the supplementary material with a link to a repository.

References

- Acevedo, J., Fernández-Viejo, G., Llana-Fúnez, S., López-Fernández, C., Olona, J., Pérez-Millán, D., 2022. Radial anisotropy and S-wave velocity depict the internal to external zone transition within the Variscan orogen (NW Iberia). *Solid Earth* 13, 659–679. <https://doi.org/10.5194/se-13-659-2022>.
- Anderson, D.L., 1961. Elastic wave propagation in layered anisotropic media. *J. Geophys. Res.* 1896–1977 (66), 2953–2963. <https://doi.org/10.1029/JZ066i009p02953>.
- Asaka, M., Holt, R.M., Bakk, A., 2021. Rock physics model of shale: predictive aspect. *J. Geophys. Res. Solid Earth* 126, e2021JB021993. <https://doi.org/10.1029/2021JB021993>.
- Bachmann, F., Hielscher, R., Schaeben, H., 2010. Texture analysis with MTEX – free and open source software toolbox. *Solid State Phenom.* 160, 63–68. <https://doi.org/10.4028/www.scientific.net/SSP.160.63>.
- Barrool, G., Mainprice, D., 1993. A quantitative evaluation of the contribution of crustal rocks to the shear-wave splitting of teleseismic SKS waves. *Phys. Earth Planet. Inter.* 78, 281–300. [https://doi.org/10.1016/0031-9201\(93\)90161-2](https://doi.org/10.1016/0031-9201(93)90161-2).
- Barrool, G., Souriau, A., Vauchez, A., Diaz, J., Gallart, J., Tubia, J., Cuevas, J., 1998. Lithospheric anisotropy beneath the Pyrenees from shear wave splitting. *J. Geophys. Res. Solid Earth* 103, 30039–30053. <https://doi.org/10.1029/98JB02790>.
- Bass, J.D., 2013. Elasticity of Minerals, Glasses, and Melts. In: Ahrens, T.J. (Ed.), AGU Reference Shelf. American Geophysical Union, Washington, D. C, pp. 45–63. <https://doi.org/10.1029/RF002p0045>.
- Bozzolo, N., Gerspach, F., Sawina, G., Wagner, F., 2007. Accuracy of orientation distribution function determination based on EBSD data—a case study of a recrystallized low alloyed Zr sheet. *J. Microsc.* 227, 275–283. <https://doi.org/10.1111/j.1365-2818.2007.01811.x>.
- Browaeys, J.T., Chevrot, S., 2004. Decomposition of the elastic tensor and geophysical applications. *Geophys. J. Int.* 159, 667–678. <https://doi.org/10.1111/j.1365-246X.2004.02415.x>.
- Brown, J.M., Abramson, E.H., Angel, R.J., 2006. Triclinic elastic constants for low albite. *Phys. Chem. Miner.* 33, 256–265. <https://doi.org/10.1007/s00269-006-0074-1>.
- Bunge, H.-J., 1982. *Texture Analysis in Materials Science: Mathematical Methods*. Elsevier.
- Cárdenes, V., Lopez-Sánchez, M.A., Barou, F., Olona, J., Llana-Fúnez, S., 2021. Crystallographic preferred orientation, seismic velocity and anisotropy in roofing slates. *Tectonophysics* 808, 228815. <https://doi.org/10.1016/j.tecto.2021.228815>.
- Cholach, P.Y., Schmitt, D.R., 2006. Intrinsic elasticity of a textured transversely isotropic muscovite aggregate: comparison to the seismic anisotropy of schists and shales. *J. Geophys. Res.* 111, 2005JB004158. <https://doi.org/10.1029/2005JB004158>.
- Cholach, P.Y., Molyneux, J.B., Schmitt, D.R., 2005. Flin Flon Belt seismic anisotropy: elastic symmetry, heterogeneity, and shear-wave splitting. *Can. J. Earth Sci.* 42, 533–554. <https://doi.org/10.1139/e04-094>.
- Christensen, N.I., Mooney, W.D., 1995. Seismic velocity structure and composition of the continental crust: a global view. *J. Geophys. Res.* 100, 9761–9788. <https://doi.org/10.1029/95JB00259>.
- Díaz, J., Gallart, J., Ruiz, M., Pulgar, J.A., López-Fernández, C., González-Cortina, J.M., 2006. Probing seismic anisotropy in North Iberia from shear wave splitting. *Phys. Earth Planet. Interiors* 158, 210–225. <https://doi.org/10.1016/j.pepi.2005.12.011>.
- Fettes, D., Desmons, J., 2011. *Metamorphic Rocks: A Classification and Glossary of Terms*. Cambridge University Press.
- Godfrey, N.J., Christensen, N.I., Okaya, D.A., 2000. Anisotropy of schists: contribution of crustal anisotropy to active source seismic experiments and shear wave splitting observations. *J. Geophys. Res.* 105, 27991–28007. <https://doi.org/10.1029/2000JB900286>.
- Guo, B.-B., Wang, H.-C., Zhao, W.-H., Ji, S., Sun, D.-S., Li, A.W., Long, C.-X., 2014. Analysis of seismic anisotropy of the typical slate from the Gaoligong Mountains, Yunnan Province, China. *Chin. J. Geophys.* 57, 154–165. <https://doi.org/10.1002/cjg2.20093>.
- Hielscher, R., 2013. Kernel density estimation on the rotation group and its application to crystallographic texture analysis. *J. Multivar. Anal.* 119, 119–143. <https://doi.org/10.1016/j.jmva.2013.03.014>.
- Hielscher, R., Schaeben, H., 2008. A novel pole figure inversion method: specification of the MTEX algorithm. *J. Appl. Crystallogr.* 41, 1024–1037. <https://doi.org/10.1107/S0021889808030112>.
- Hielscher, R., Schaeben, H., Chateigner, D., 2007. On the entropy to texture index relationship in quantitative texture analysis. *J. Appl. Crystallogr.* 40, 371–375. <https://doi.org/10.1107/S0021889806055476>.
- Hill, R., 1952. The elastic behaviour of a crystalline aggregate. *Proc. Phys. Soc. A* 65, 349–354. <https://doi.org/10.1088/0370-1298/65/5/307>.
- Hornby, B.E., 1998. Experimental laboratory determination of the dynamic elastic properties of wet, drained shales. *J. Geophys. Res. Solid Earth* 103, 29945–29964. <https://doi.org/10.1029/97JB02380>.
- Horne, S.A., 2013. A statistical review of mudrock elastic anisotropy. *Geophys. Prospect.* 61, 817–826. <https://doi.org/10.1111/1365-2478.12036>.
- Ivankina, T.I., Zel, I.Yu., Lokajicek, T., Kern, H., Lobanov, K.V., Zharikov, A.V., 2017. Elastic anisotropy of layered rocks: ultrasonic measurements of plagioclase-biotite-muscovite (sillimanite) gneiss versus texture-based theoretical predictions (effective media modeling). *Tectonophysics* 712–713, 82–94. <https://doi.org/10.1016/j.tecto.2017.05.005>.
- Ji, S., Li, A., Wang, Q., Long, C., Wang, H., Marcotte, D., Salisbury, M., 2013. Seismic velocities, anisotropy, and shear-wave splitting of antigorite serpentinites and tectonic implications for subduction zones. *JGR Solid Earth* 118, 1015–1037. <https://doi.org/10.1002/jgrb.50110>.
- Ji, S., Shao, T., Michibayashi, K., Oya, S., Satsukawa, T., Wang, Q., Zhao, W., Salisbury, M.H., 2015. Magnitude and symmetry of seismic anisotropy in mica- and amphibole-bearing metamorphic rocks and implications for tectonic interpretation of seismic data from the southeast Tibetan Plateau. *JGR Solid Earth* 120, 6404–6430. <https://doi.org/10.1002/2015JB012209>.
- Johnston, J.E., Christensen, N.I., 1995. Seismic anisotropy of shales. *J. Geophys. Res. Solid Earth* 100, 5991–6003. <https://doi.org/10.1029/95JB00031>.
- Jung, H., 2011. Seismic anisotropy produced by serpentine in mantle wedge. *Earth Planet. Sci. Lett.* 307, 535–543. <https://doi.org/10.1016/j.epsl.2011.05.041>.
- Katahara, K.W., 1996. Clay mineral elastic properties. In: SEG Technical Program Expanded Abstracts 1996. Society of Exploration Geophysicists, pp. 1691–1694. <https://doi.org/10.1190/1.1826454>.
- Katayama, I., Hirauchi, K., Michibayashi, K., Ando, J., 2009. Trench-parallel anisotropy produced by serpentine deformation in the hydrated mantle wedge. *Nature* 461, 1114–1117. <https://doi.org/10.1038/nature08513>.
- Kern, H., Lokajicek, T., Svitek, T., Wenk, H., 2015. Seismic anisotropy of serpentinite from Val Malenco, Italy. *JGR Solid Earth* 120, 4113–4129. <https://doi.org/10.1002/2015JB012030>.
- Kube, C.M., 2016. Elastic anisotropy of crystals. *AIP Adv.* 6, 095209. <https://doi.org/10.1063/1.4962996>.

- Lee, J., Mookherjee, M., Kim, T., Jung, H., Klemd, R., 2021. Seismic anisotropy in subduction zones: evaluating the role of chloritoid. *Front. Earth Sci.* 9. <https://doi.org/10.3389/feart.2021.644958>.
- Lloyd, G.E., Butler, R.W.H., Casey, M., Mainprice, D., 2009. Mica, deformation fabrics and the seismic properties of the continental crust. *Earth Planet. Sci. Lett.* 288, 320–328. <https://doi.org/10.1016/j.epsl.2009.09.035>.
- Lonardelli, I., Wenk, H.-R., Ren, Y., 2007. Preferred orientation and elastic anisotropy in shales. *Geophysics* 72, D33–D40. <https://doi.org/10.1190/1.2435966>.
- Mainprice, D., Casey, M., 1990. The calculated seismic properties of quartz mylonites with typical fabrics: relationship to kinematics and temperature. *Geophys. J. Int.* 103, 599–608. <https://doi.org/10.1111/j.1365-246X.1990.tb05674.x>.
- Mainprice, D., Humbert, M., 1994. Methods of calculating petrophysical properties from lattice preferred orientation data. *Surv. Geophys.* 15, 575–592. <https://doi.org/10.1007/BF00690175>.
- Mainprice, D., Hielscher, R., Schaeben, H., 2011. Calculating anisotropic physical properties from texture data using the MTEX open-source package. *Geol. Soc. Lond. Spec. Publ.* 360, 175–192. <https://doi.org/10.1144/SP360.10>.
- Mainprice, D., Bachmann, F., Hielscher, R., Schaeben, H., 2015. Descriptive tools for the analysis of texture projects with large datasets using MTEX: strength, symmetry and components. *Geol. Soc. Lond. Spec. Publ.* 409, 251–271. <https://doi.org/10.1144/SP409.8>.
- Meltzer, A., Christensen, N., 2001. Nanga Parbat crustal anisotropy: implications for interpretation of crustal velocity structure and shear-wave splitting. *Geophys. Res. Lett.* 28, 2129–2132. <https://doi.org/10.1029/2000GL012262>.
- Militzer, B., Wenk, H.-R., Stackhouse, S., Stixrude, L., 2011. First-principles calculation of the elastic moduli of sheet silicates and their application to shale anisotropy. *Am. Mineral.* 96, 125–137. <https://doi.org/10.2138/am.2011.3558>.
- Mookherjee, M., Mainprice, D., 2014. Unusually large shear wave anisotropy for chlorite in subduction zone settings. *Geophys. Res. Lett.* 41, 1506–1513. <https://doi.org/10.1002/2014GL059334>.
- Naus-Thijssen, F.M.J., Goupee, A.J., Johnson, S.E., Vel, S.S., Gerbi, C., 2011a. The influence of crenulation cleavage development on the bulk elastic and seismic properties of phyllosilicate-rich rocks. *Earth Planet. Sci. Lett.* 311, 212–224. <https://doi.org/10.1016/j.epsl.2011.08.048>.
- Naus-Thijssen, F.M.J., Goupee, A.J., Vel, S.S., Johnson, S.E., 2011b. The influence of microstructure on seismic wave speed anisotropy in the crust: computational analysis of quartz-muscovite rocks. *Geophys. J. Int.* 185, 609–621. <https://doi.org/10.1111/j.1365-246X.2011.04978.x>.
- Ranganathan, S.I., Ostoja-Starzewski, M., 2008. Universal elastic anisotropy index. *Phys. Rev. Lett.* 101, 055504. <https://doi.org/10.1103/PhysRevLett.101.055504>.
- Sayers, C.M., 2005. Seismic anisotropy of shales. *Geophys. Prospect.* 53, 667–676. <https://doi.org/10.1111/j.1365-2478.2005.00495.x>.
- Sayers, C.M., den Boer, L.D., 2020. Effect of variations in microstructure on clay elastic anisotropy. *Geophysics* 85, MR73–MR82. <https://doi.org/10.1190/geo2019-0374.1>.
- Schaeben, H., 1988. Entropy optimization in texture goniometry. I. Methodology. *Phys. Status Solidi B* 148, 63–72. <https://doi.org/10.1002/pssb.2221480104>.
- Thomsen, L., 1986. Weak elastic anisotropy. *Geophysics* 51, 1954–1966. <https://doi.org/10.1190/1.1442051>.
- Thomsen, L., Anderson, D.L., 2015. Weak elastic anisotropy in global seismology. In: Foulger, G.R., Lustrino, M., King, S.D. (Eds.), *The Interdisciplinary Earth: A Volume in Honor of Don L. Anderson*. Geological Society of America, p. 0. [https://doi.org/10.1130/2015.2514\(04\)](https://doi.org/10.1130/2015.2514(04)).
- Waeselmann, N., Brown, J.M., Angel, R.J., Ross, N., Zhao, J., Kaminsky, W., 2016. The elastic tensor of monoclinic alkali feldspars. *Am. Mineral.* 101, 1228–1231. <https://doi.org/10.2138/am-2016-5583>.
- Wagner, F., Matthies, S., Van Landuyt, O., 1998. Processing Individual Orientation Data to Calculate ODFs. *MSF* 273–275, pp. 89–98. <https://doi.org/10.4028/www.scientific.net/MSF.273-275.89>.
- Wang, J., Mao, Z., Jiang, F., Duffy, T.S., 2015. Elasticity of single-crystal quartz to 10 GPa. *Phys. Chem. Miner.* 42, 203–212. <https://doi.org/10.1007/s00269-014-0711-z>.
- Ward, D., Mahan, K., Schulte-Pelkum, V., 2012. Roles of quartz and mica in seismic anisotropy of mylonites: roles of quartz and mica. *Geophys. J. Int.* 190, 1123–1134. <https://doi.org/10.1111/j.1365-246X.2012.05528.x>.
- Wenk, H.-R., Yu, R., Cárdenes, V., Lopez-Sánchez, M.A., Sintubin, M., 2020. Fabric and anisotropy of slates: from classical studies to new results. *J. Struct. Geol.* 138, 104066. <https://doi.org/10.1016/j.jsg.2020.104066>.
- Wenk, H.-R., Huang, J., Devoe, M., Gómez-Barreiro, J., Vasin, R., Ren, Y., Barrios-Sánchez, S., 2022. Crystallographic and shape preferred orientation producing anisotropy in slates from Northern Spain. *J. Struct. Geol.* 164, 104730. <https://doi.org/10.1016/j.jsg.2022.104730>.
- Wenk, H.-R., Kattemalavadi, A., Zhang, Y., Kennedy, E.R., Borkiewicz, O., 2025. Exploring microstructures and anisotropies of serpentinites. *Contrib. Mineral. Petro.* 180, 23. <https://doi.org/10.1007/s00410-025-02209-5>.
- Yurikov, A., Pervukhina, M., Beloborodov, R., Delle Piane, C., Dewhurst, D.N., Lebedev, M., 2021. Modeling of compaction trends of anisotropic elastic properties of shales. *J. Geophys. Res. Solid Earth* 126, e2020JB019725. <https://doi.org/10.1029/2020JB019725>.